EPJ manuscript No.
(will be inserted by the editor)

CT-MQC – A Coupled-Trajectory Mixed Quantum/Classical method including nonadiabatic quantum coherence effects

Basile F. E. Curchod[1], Federica Agostini[2], and Ivano Tavernelli[3,4]

[1] Department of Chemistry, Durham University, South Road, Durham DH1 3LE, United Kingdom
[2] Laboratoire de Chimie Physique, UMR 8000 CNRS/University Paris-Sud, 91405 Orsay, France
[3] IBM Research GmbH, Zürich Research Laboratory, 8803 Rüschlikon, Switzerland
[4] ita@zurich.ibm.com

Received: date / Revised version: date

Abstract. Upon photoexcitation by a short light pulse, molecules can reach regions of the configuration space characterized by strong *nonadiabaticity*, where the motion of the nuclei is strongly coupled to the motion of the electrons. The subtle interplay between the nuclear and electronic degrees of freedom in such situations is rather challenging to capture by state-of-the-art nonadiabatic dynamics approaches, limiting therefore their predictive power. The Exact Factorization of the molecular wavefunction, though, offers new perspectives in the solution of this longstanding issue. Here, we investigate the performance of a mixed quantum/classical (MQC) limit of this theory, named Coupled Trajectory-MQC, which was shown to reproduce the excited-state dynamics of small systems accurately. The method is applied to the study of the photoinduced ring opening of oxirane and the results are compared with two other nonadiabatic approaches based on different Ansätze for the molecular wavefunction, namely Ehrenfest dynamics and Ab Initio Multiple Spawning (AIMS). All simulations were performed using linear-response time-dependent density functional theory. We show that the CT-MQC method can capture the (de)coherence effects resulting from the dynamics through conical intersections, in good agreement with the results obtained with AIMS and in contrast with ensemble Ehrenfest dynamics.

PACS. XX.XX.XX No PACS code given

1 Introduction

In the field of quantum dynamics, trajectory-based schemes are perhaps the most powerful simulation approaches to get a glimpse at the dynamics of molecules. Microscopic systems are governed by quantum mechanics, but unfortunately a full quantum dynamical treatment of molecules is presently not computationally tractable when it goes beyond a few degrees of freedom. A trajectory-based approach, instead, offers access to a wide range of processes and properties at the cost of providing only an approximate solution to the problem. When describing time-dependent phenomena in molecules, classical trajectories are generally used to reproduce the evolution of the nuclei, while electrons are treated quantum mechanically. This strategy is computationally advantageous, as it allows for the calculation of electronic properties, *i.e.*, ground- and excited-state energies, forces, and couplings, only for the nuclear configurations visited during the dynamics. The numerical advantage of trajectory-based approaches is, however, confronted with a very fundamental and still highly debated issue [1,2]: how can classical nuclei be properly coupled, dynamically, to quantum-mechanical electrons? Other than being an intriguing theoretical challenge in itself, this issue has also important practical implications related to the description of inherently quantum mechanical properties, such as decoherence, dephasing, or interferences [3–5], by means of trajectory-based approaches.

In the adiabatic case, *i.e.*, in the Born-Oppenheimer (BO) regime [6], the procedure for coupling classically-moving nuclei and quantum mechanical electrons is well-established: by "freezing" the electrons in their ground state, their coupling to the nuclear motion can be described by a potential energy contribution to the nuclear Hamiltonian. However, the BO picture is only valid as far as the system of interest does not visit regions of the configuration space with a small, or eventually vanishing, energy gap between electronic states [7]. Improvements to this approximation have been proposed in the literature [8–10], still maintaining the very intuitive picture of classical nuclei moving on a single potential energy surface (PES). Beyond the adiabatic regime, this simple representation does not hold any longer (in the BO framework): the PESs become strongly coupled in regions where the corresponding electronic states are close or degenerate in energy. Several trajectory-based schemes [11–29,1,30–39] have been devised to guide classical trajectories in the

presence of such nonadiabatic couplings. Trajectories can for instance hop and switch from one adiabatic PES to another [15], can evolve on a mean-field potential [17,16], or can spawn in region of strong nonadiabatic coupling inducing coupling among them [34]. From all these studies it emerges that within the post-Born-Oppenheimer picture there is no unique and unambiguous definition of a trajectory-based classical limit of nuclear dynamics.

Recently, the concept of an *exact force* that drives the (classical) nuclear dynamics in nonadiabatic conditions rose [40–42] from the framework of the exact factorization of the electron-nuclear wavefunction [43,44]. Starting from the quantum-mechanical, fully interacting electron-nuclear problem, a time-dependent Schrödinger equation for a nuclear wavefunction can be derived, and time-dependent scalar and vector potentials now completely account for electron-nuclear coupling effects, allowing to unambiguously define the classical forces acting on the nuclei. The exact-factorization framework has been employed to derive the coupled-trajectory mixed quantum-classical (CT-MQC) scheme [45,18,46], that makes use of the time-dependent potentials to determine an approximation to the exact nuclear forces and to guide trajectories through regions of strong nonadiabaticity.

In this paper, we employ CT-MQC dynamics to analyze the photoactivated ring-opening of the molecule oxirane. In a previous work [46], we described this process by means of CT-MQC dynamics and compared the results with trajectory surface hopping [15,47], stressing the ability of the new algorithm to capture quantum decoherence effects [48,47,49–53,47,54–58]. In the following, we aim at investigating in more detail the same photochemical process with the CT-MQC approach and validate, as far as it is possible, our observations with results obtained using Ab Initio Multiple Spawning (AIMS) [36]. Both methods have the interesting property of incorporating all quantum mechanical coherence/decoherence effects of the nuclear wavepacket dynamics. In addition, some of the CT-MQC results will also be compared to ensemble Ehrenfest dynamics [59], in order to shed further light on the relevance of the coupling among trajectories. We start in Section 2 by briefly recalling the exact factorization and the procedure leading to the derivation of the CT-MQC quantum-classical equations, which is the main focus of this work. AIMS is introduced in Section 3 and is used to compare and rationalize the CT-MQC results. Numerical details are provided in Section 4, whereas our analysis of the photoinduced ring-opening process in oxirane is discussed in Section 5. Conclusions are summarized in Section 6.

2 The exact factorization and its quantum-classical approximation

The time-dependent molecular wavefunction, $\Psi(\mathbf{r},\mathbf{R},t)$, is the solution of the time-dependent Schrödinger equation (TDSE) $\hat{H}\Psi = i\hbar\partial_t\Psi$, with Hamiltonian $\hat{H}(\mathbf{r},\mathbf{R}) = \hat{T}_n(\mathbf{R}) + \hat{H}_{BO}(\mathbf{r},\mathbf{R})$, containing the nuclear kinetic energy, $\hat{T}_n$, and the electronic Born-Oppenheimer (BO) Hamiltonian, $\hat{H}_{BO}$, defined as the sum of the electronic kinetic energy and of the interaction potentials. Here, the symbols $\mathbf{r},\mathbf{R}$ indicate all electronic and nuclear coordinates, respectively. The full wavefunction can be exactly written [43,44] as the product

$$\Psi(\mathbf{r},\mathbf{R},t) = \chi(\mathbf{R},t)\Phi_{\mathbf{R}}(\mathbf{r},t), \tag{1}$$

with $\chi(\mathbf{R},t)$ the nuclear wavefunction, yielding the exact nuclear many-body density (and current density), and $\Phi_{\mathbf{R}}(\mathbf{r},t)$ an electronic factor that parametrically depends on the nuclear configuration. To guarantee that $|\chi(\mathbf{R},t)|^2$ reproduces at all times the nuclear density, the partial normalization condition $\int d\mathbf{r}|\Phi_{\mathbf{R}}(\mathbf{r},t)|^2 = 1\ \forall\,\mathbf{R},t$ is imposed.

When inserted into the TDSE, and by using the partial normalization condition [60,61], the exact factorization given in Eq. (1) yields coupled evolution equations for the two components of the molecular wavefunction, namely

$$\left[\hat{H}_{BO} + \hat{U}_{en}^{coup} - \epsilon\right]\Phi_{\mathbf{R}}(\mathbf{r},t) = i\hbar\partial_t\Phi_{\mathbf{R}}(\mathbf{r},t) \tag{2}$$

$$\left[\sum_{\nu=1}^{N_n}\frac{[-i\hbar\nabla_\nu + \mathbf{A}_\nu]^2}{2M_\nu} + \epsilon\right]\chi(\mathbf{R},t) = i\hbar\partial_t\chi(\mathbf{R},t). \tag{3}$$

Nuclear masses are indicated by the symbol M_ν, with the index ν running over the N_n nuclei. In the electronic equation (2), the electron-nuclear coupling operator $\hat{U}_{en}^{coup}[\Phi_{\mathbf{R}},\chi]$ [62,63] couples the electronic evolution to the nuclear dynamics, as it depends on the nuclear wavefunction,

$$\hat{U}_{en}^{coup}[\Phi_{\mathbf{R}},\chi] = \sum_{\nu=1}^{N_n}\frac{1}{M_\nu}\left[\frac{[-i\hbar\nabla - \mathbf{A}_\nu]^2}{2} + \left(\frac{-i\hbar\nabla_\nu\chi}{\chi} + \mathbf{A}_\nu\right)(-i\hbar\nabla_\nu - \mathbf{A}_\nu)\right]. \tag{4}$$

The scalar potential, or time-dependent potential energy surface (TDPES) [40–42,64–69], $\epsilon(\mathbf{R},t)$, and the time-dependent vector potential [65,8,10,70,71,9], $\mathbf{A}_\nu(\mathbf{R},t)$, are defined as

$$\epsilon(\mathbf{R},t) = \langle\Phi_{\mathbf{R}}(t)|\,\hat{H}_{BO} + \hat{U}_{en}^{coup} - i\hbar\partial_t\,|\Phi_{\mathbf{R}}(t)\rangle_{\mathbf{r}}\,, \tag{5}$$

and

$$\mathbf{A}_\nu(\mathbf{R},t) = \langle\Phi_{\mathbf{R}}(t)|\,-i\hbar\nabla_\nu\Phi_{\mathbf{R}}(t)\rangle_{\mathbf{r}}\,, \tag{6}$$

respectively. The symbol $\langle\cdot\rangle_{\mathbf{r}}$ stands for an integration over electronic coordinates. In the nuclear TDSE (Eq. (3)), the time-dependent potentials fully account for electronic nonadiabatic effects, *i.e.*, excited-state effects, on nuclear motion.

The product form of the molecular wavefunction, Eq. (1), is clearly invariant under a $(\mathbf{R},t)$-dependent phase transformation of the electronic and nuclear components. Therefore, uniqueness of the solution of Eqs. (2) and (3) is guaranteed only by choosing a condition to fix the gauge freedom.

If the nuclear wavefunction is written in polar form, that is, $\chi(\mathbf{R},t) = \exp[(i/\hbar)S(\mathbf{R},t)]\,|\chi(\mathbf{R},t)|$, the nuclear TDSE (Eq. (3)) yields the coupled evolution equations for the phase

$$\partial_t S = -\left[\sum_\nu \frac{[\nabla_\nu S + \mathbf{A}_\nu]^2}{2M_\nu} + \epsilon\right] - \sum_\nu \frac{-\hbar^2}{2M_\nu}\frac{\nabla_\nu^2|\chi|}{|\chi|} \quad (7)$$

and for the density $\Gamma(\mathbf{R},t) = |\chi(\mathbf{R},t)|^2$

$$\partial_t \Gamma = -\sum_\nu \nabla_\nu \cdot \left(\frac{\nabla_\nu S + \mathbf{A}_\nu}{M_\nu}\,\Gamma\right), \quad (8)$$

of the wavefunction. Neglecting the last term in Eq. (7), this Hamilton-Jacobi equation can be solved independently from the continuity equation (Eq. (8)). We determine the characteristics of the Hamilton-Jacobi equation (Eq. (7)), that are, as it is well-known [72], generated by classical Hamilton's equations

$$\dot{\mathbf{R}}_\nu = \frac{\mathbf{P}_\nu + \mathbf{A}_\nu}{M_\nu} = \frac{\widetilde{\mathbf{P}}_\nu}{M_\nu} \quad \text{for } \nu = 1,\dots,N_n \quad (9)$$

$$\dot{\widetilde{\mathbf{P}}}_\nu = -\nabla_\nu\left(\epsilon + \sum_{\nu'=1}^{N_n} \dot{\mathbf{R}}_{\nu'}\cdot\mathbf{A}_{\nu'}\right) + \dot{\mathbf{A}}_\nu. \quad (10)$$

The gauge freedom is fixed by the condition $\epsilon + \sum_{\nu'}\dot{\mathbf{R}}_{\nu'}\cdot\mathbf{A}_{\nu'} = 0$.

The trajectories generated by Eqs. (9) and (10) are coupled to the electronic equation (Eq. (2)) where the (conditional) electronic wavefunction $\Phi_{\mathbf{R}}(\mathbf{r},t)$ is expanded in the adiabatic basis, *i.e.*, in the basis formed by the eigenstates of the BO Hamiltonian $\hat{H}_{BO}$. With this final ingredient, the CT-MQC equations are

$$\dot{\mathbf{R}}_\nu^{(I)}(t) = \frac{\widetilde{\mathbf{P}}_\nu^{(I)}(t)}{M_\nu} \quad (11)$$

$$\dot{\widetilde{\mathbf{P}}}_\nu^{(I)}(t) = \mathbf{F}_{\nu,\mathrm{Eh}}^{(I)}(t) + \mathbf{F}_{\nu,\mathrm{qm}}^{(I)}(t) \quad (12)$$

$$\dot{C}_k^{(I)}(t) = \dot{C}_{k,\mathrm{Eh}}^{(I)}(t) + \dot{C}_{k,\mathrm{qm}}^{(I)}(t). \quad (13)$$

All $\mathbf{R}$-dependent quantities have been labeled by an index (I), indicating their dependence on the position of the trajectory: these equations are solved along a trajectory, or characteristic, (I). The symbol $C_k^{(I)}(t)$, with $k = 1,\dots,n$, stands for the position-dependent coefficients of the expansion of the electronic wavefunction $\Phi_{\mathbf{R}}(\mathbf{r},t)$ on the n adiabatic states. A detailed derivation of these equations and the underlying approximations can be found in Refs. [18,46].

Eqs. (12) and (13) have been decomposed as the sum of two terms, respectively labeled *Eh* and *qm*. The former are Ehrenfest-like terms, specifically,

$$\mathbf{F}_{\nu,\mathrm{Eh}}^{(I)} = -\sum_k \left|C_k^{(I)}\right|^2 \nabla_\nu \epsilon_{BO}^{(k),(I)} - \sum_{k,l} C_l^{(I)*} C_k^{(I)} \left(\epsilon_{BO}^{(k),(I)} - \epsilon_{BO}^{(l),(I)}\right)\mathbf{d}_{lk,\nu}^{(I)} \quad (14)$$

and

$$\dot{C}_{k,\mathrm{Eh}}^{(I)} = -\frac{i}{\hbar}\epsilon_{BO}^{(k),(I)} C_k^{(I)} - \sum_{\nu=1}^{N_n}\dot{\mathbf{R}}_\nu^{(I)}\cdot\sum_l \mathbf{d}_{kl,\nu}^{(I)} C_l^{(I)}. \quad (15)$$

The eigenvalues of the BO Hamiltonian are indicated by the symbol $\epsilon_{BO}^{(k),(I)}$. They are the adiabatic, or BO, PESs evaluated along the trajectory; the coupling among the electronic states is given by the nonadiabatic coupling vectors $\mathbf{d}_{kl,\nu}^{(I)}$. The latter terms in Eqs. (12) and (13) depend on the quantum momentum $\mathbf{Q}_\nu(\mathbf{R},t)$, defined via

$$\frac{-i\hbar\nabla_\nu\chi}{\chi} + \mathbf{A}_\nu = (\nabla_\nu S + \mathbf{A}_\nu) + i\frac{-\hbar\nabla_\nu|\chi|^2}{2|\chi|^2} \quad (16)$$

$$= M_\nu\dot{\mathbf{R}}_\nu + i\mathbf{Q}_\nu, \quad (17)$$

which appears in Eq. (4). Their expressions are

$$\mathbf{F}_{\nu,\mathrm{qm}}^{(I)} = \sum_k \left|C_k^{(I)}\right|^2 \left(\sum_{\nu'=1}^{N_n}\frac{2\mathbf{Q}_{\nu'}^{(I)}}{\hbar M_{\nu'}}\cdot\mathbf{f}_{l,\nu'}^{(I)}\right) \times\left[\mathbf{f}_{k,\nu}^{(I)} - \sum_l \left|C_l^{(I)}\right|^2\mathbf{f}_{l,\nu}^{(I)}\right] \quad (18)$$

$$\dot{C}_{k,\mathrm{qm}}^{(I)} = \sum_{\nu=1}^{N_n}\frac{\mathbf{Q}_\nu^{(I)}}{\hbar M_\nu}\cdot\left[\mathbf{f}_{k,\nu}^{(I)} - \sum_l\left|C_l^{(I)}\right|^2\mathbf{f}_{l,\nu}^{(I)}\right]C_k^{(I)}, \quad (19)$$

with the $\mathbf{R}$-dependent quantum momentum evaluated at the position of the trajectory, $\mathbf{Q}_\nu(\mathbf{R},t) \to \mathbf{Q}_\nu^{(I)}(t)$, and with $\mathbf{f}_{k,\nu}^{(I)}(t) = \int^t[-\nabla_\nu\epsilon_{BO}^{(k),(I)}]dt'$, the integral over time of the adiabatic force, implicitly depending on time via the dependence on the trajectory.

3 Ab Initio Multiple Spawning

Full Multiple Spawning (FMS) [32–34,19,35,36,38,73] employs a Born-Huang representation of the molecular wavefunction and portrays the nuclear dynamics by using a swarm of *coupled* frozen multidimensional Gaussians [74]. The Gaussians follow classical trajectories and their number can be adapted during the dynamics to ensure a proper support to the nuclear wavepacket propagation. Within this picture, the Born-Huang representation reads

$$\Psi(\boldsymbol{r},\boldsymbol{R},t) = \sum_k\sum_I^{N_{TBFs,k}} \tilde{C}_I^{(k)}(t) \times\tilde{\chi}_I^{(k)}\left(\boldsymbol{R};\overline{\boldsymbol{R}}_I^{(k)}(t),\overline{\boldsymbol{P}}_I^{(k)}(t),\overline{\gamma}_I^{(k)}(t),\boldsymbol{\alpha}\right)\varphi_{\boldsymbol{R}}^{(k)}(\boldsymbol{r}), \quad (20)$$

where $\tilde{\chi}_I^{(k)}\left(\boldsymbol{R};\overline{\boldsymbol{R}}_I^{(k)}(t),\overline{\boldsymbol{P}}_I^{(k)}(t),\overline{\gamma}_I^{(k)}(t),\boldsymbol{\alpha}\right)$ are the trajectory basis functions (TBFs) I evolving on state (k) with mean position $\overline{\boldsymbol{R}}_I^{(k)}(t)$, momentum $\overline{\boldsymbol{P}}_I^{(k)}(t)$, phase $\overline{\gamma}_I^{(k)}(t)$, and frozen width $\boldsymbol{\alpha}$. $\tilde{C}_I^{(k)}(t)$ is the complex coefficient for

the TBF I evolving on electronic state (k). The TDSE can be rewritten in the basis of the TBFs, leading to a set of coupled equations of motion for the complex coefficients. It is important to note that the number of TBFs can be extended every time a nonadiabatic coupling is detected, ensuring an accurate description of the nuclear amplitude transfer between electronic states resulting from nonadiabaticity (more details on the spawning algorithms can be found in Refs. [36,75,73]). If a sufficiently large number of TBFs is used, FMS is formally exact. However, it requires the evaluation of multidimensional Gaussian integrals including electronic quantities like energies or nonadiabatic couplings, meaning that FMS is not directly suitable for ab initio nonadiabatic molecular dynamics.

Ab Initio Multiple Spawning (AIMS) proposes to approximate the coupling between TBFs in two different ways: the integrals are approximated by expanding any electronic quantity in a Taylor expansion of order zero (saddle point approximation) and the TBFs employed to describe the nuclear wavepacket at time $t = 0$ (the parent TBFs) are considered uncoupled (independent first generation approximation, IFGA). For details and discussions on these two approximations, the reader is referred to Refs. [36,76,73]. AIMS has been coupled with different electronic-structure methods such as SA-CASSCF [77,78], MS-CASPT2 [79], FOMO-CASCI [80], or linear-response TDDFT (LR-TDDFT) [81].

4 Computational details

CT-MQC and Ehrenfest calculations are performed with the plane-waves based electronic structure package CPMD [82], employing the PBE [83] functional for ground-state and excited-state calculations. LR-TDDFT calculations [84–86] are based on the Tamm-Dancoff approximation [87,88] (TDA). While the adiabatic approximation [89], inherent to a practical use of LR-TDDFT, precludes an accurate description of conical intersections between S_1 and S_0 [90], the dynamics presented here is only concerned with the coupling between the excited states S_1 and S_2. Conical intersections between excited states are adequately captured by LR-TDDFT, even within the adiabatic approximation. For more information on this subject, we refer to Ref. [89,91]. Furthermore, studies have showed that, for the case of oxirane, LR-TDDFT with the TDA provides a good description of the S_1/S_0 branching plane [91]. The Kleinman-Bylander [92] pseudo-potential has been used for all atom species together with a plane-wave cutoff of 70 Ry. Initial conditions, *i.e.*, positions and momenta, have been sampled from an ab initio ground-state trajectory of 2 ps at 300 K. $N_{tr} = 100$ trajectories are propagated with a time step of 0.12 fs (5 a.u.). The Ehrenfest dynamics was obtained by using the CT-MQC algorithm implemented in CPMD while neglecting the qm terms in the equations for the force, Eq. (12), as well as in the evolution equation for the BO coefficients, Eq. (13).

The populations of the electronic adiabatic states are estimated via the expression

$$\rho_k(t) = \frac{1}{N_{tr}} \sum_{I=1}^{N_{tr}} \left| C_k^{(I)}(t) \right|^2 \text{ with } k = 0, 1, 2, \tag{21}$$

that is an average of the populations associated to each trajectory (I). In Section 5 we will also report the indicator of decoherence [45,18,46], defined by the expression

$$\eta_{kl}(t) = \frac{1}{N_{tr}} \sum_{I=1}^{N_{tr}} \left| C_k^{(I)\,*}(t) C_l^{(I)}(t) \right|^2 . \tag{22}$$

The quantum-mechanical (exact) expression corresponding to Eq. (22) is

$$\eta_{kl}^{\text{ex.}}(t) = \int d\mathbf{R} \left| C_k^*(\mathbf{R}, t) C_l(\mathbf{R}, t) \right|^2 \left| \chi(\mathbf{R}, t) \right|^2 . \tag{23}$$

The relation between the two expressions can be easily derived by replacing the nuclear density with its "classical" expression as a sum of δ-functions centered at the positions of the trajectories, *i.e.*, $|\chi(\mathbf{R}, t)|^2 = (N_{tr})^{-1} \sum_I \delta(\mathbf{R} - \mathbf{R}^{(I)}(t))$. By virtue of the exact factorization (Eq. (1)), a nuclear wavepacket $\chi_l(\mathbf{R}, t)$ propagating "on" the BO PES l is $\chi_l(\mathbf{R}, t) = C_l(\mathbf{R}, t)\chi(\mathbf{R}, t)$, therefore Eq. (23) can also be written as

$$\eta_{kl}^{\text{ex.}}(t) = \int d\mathbf{R} \left| \chi_k^*(\mathbf{R}, t) \chi_l(\mathbf{R}, t) \right|^2 , \tag{24}$$

thus $\eta_{kl}^{\text{ex.}}(t)$ is clearly related to the overlap of nuclear wavepackets corresponding to different electronic states. With this definition of the decoherence indicator, decoherence can be related to the spatial separation of different wavepackets, and thus of different bundles of trajectories, "loosing memory" of each other while evolving along diverging paths.

In Section 5 we will also analyze the gauge-invariant part of the TDPES, namely

$$\epsilon_{GI}(\mathbf{R}, t) = \langle \Phi_{\mathbf{R}}(t) | \hat{H}_{BO} + \hat{U}_{en}^{coup} | \Phi_{\mathbf{R}}(t) \rangle_{\mathbf{r}} , \tag{25}$$

that translates to $\epsilon_{GI}^{(I)}(t) = \sum_k |C_k^{(I)}(t)|^2 \epsilon_{BO}^{(k),(I)}$ within the quantum-classical approximations. This quantity gives information about "which adiabatic PES" drives nuclear trajectories far away from the nonadiabatic coupling regions.

Ab Initio Multiple Spawning simulations were carried on with GPU-accelerated LR-TDDFT [93], using as for CT-MQC the PBE functional and the TDA. The initial wavepacket is composed of 20 parent TBFs, whose initial positions and momenta are similar to those employed for the CT-MQC dynamics. AIMS dynamics was performed within the IFGA and the saddle-point approximation of order zero, leading to an overall swarm of 68 TBFs. Three states were considered in the dynamics (S_0, S_1, S_2), the time step for the classical propagation is 20 a.u. (reduced to 5 a.u. in coupling regions, with the possibility to employ

an adaptive time step if required [77]). A major difference between the CT-MQC and the AIMS dynamics is found in the basis set employed for the electronic structure calculation. While CT-MQC uses the plane-wave code CPMD, AIMS is interfaced with the GPU-accelerated and Gaussian-based electronic structure code TeraChem [94–96]. Hence, all AIMS simulations are performed with a 6-31G* basis set [97] for the electronic degrees of freedom. While the state ordering is similar between the two approaches, the energy gap between the S_1 and S_2 states varies, which implies that the comparison between the two methods can only be considered *qualitative*.

In AIMS, the population of electronic state k is given by:

$$\rho_k(t) = \frac{1}{N_{IC}} \sum_{\beta=1}^{N_{IC}} \sum_{I=1,J=1}^{N_{TBFs,k}^{\beta}} \left(\tilde{C}_{I\beta}^{(k)}(t)\right)^* \tilde{C}_{J\beta}^{(k)}(t) \langle \tilde{\chi}_{I\beta}^{(k)} | \tilde{\chi}_{J\beta}^{(k)} \rangle_{\boldsymbol{R}} \,, \tag{26}$$

with N_{IC} the number of initial conditions. We also define the normalized incoherent population of a TBF I evolving on state k as

$$n_I^{(k)}(t) = \frac{\left|\tilde{C}_I^{(k)}(t)\right|^2}{\sum_k \sum_{J=1}^{N_{TBFs,k}} \left|\tilde{C}_J^{(k)}(t)\right|^2} \,. \tag{27}$$

Due to the different nature of the methods – travelling Gaussians (AIMS) *vs* trajectories (CT-MQC) – we use the approximate off-diagonal elements of the electronic density matrix as a local measure of decoherence in AIMS. These are defined as

$$\begin{aligned} \eta_{kl}^{\text{AIMS}}(t) &= \frac{1}{N_{IC}} \sum_{\beta=1}^{N_{IC}} |\langle \Psi_\beta | \varphi_{\boldsymbol{R}}^{(k)} \rangle \langle \varphi_{\boldsymbol{R}}^{(l)} | \Psi_\beta \rangle|^2 \\ &= \frac{1}{N_{IC}} \sum_{\beta=1}^{N_{IC}} \Big| \sum_{I}^{N_{TBFs,k}^{\beta}} \sum_{J}^{N_{TBFs,l}^{\beta}} \left(\tilde{C}_{I\beta}^{(k)}(t)\right)^* \tilde{C}_{J\beta}^{(l)}(t) \\ &\quad \times \langle \tilde{\chi}_{I\beta}^{(k)} | \tilde{\chi}_{J\beta}^{(l)} \rangle_{\boldsymbol{R}} \Big|^2 \,, \end{aligned} \tag{28}$$

and informs on the overlap between TBFs on the two different states k and l considered (in this case, k corresponds to S_1 and l to S_2).

While a detailed computational performance analysis of the different methods goes beyond the scope of this work, we comment here on the number of electronic structure calls required, as well as on the nature of the electronic structure properties evaluated at each call. For each nuclear integration step: (*i*) CT-MQC requires N_{tr} electronic structure calls for the calculation of the energy, the gradient and the nonadiabatic coupling vectors of all electronic states considered; (*ii*) AIMS requires $N_{TBFs} \times (N_{TBFs}+1)/2$ electronic structure calls for the calculation of the energy, the gradient and the nonadiabatic couplings associated to the single electronic state on which the TBF runs. In average, while the number of electronic structure calls in AIMS is larger than in CT-MQC, the number of electronic structure quantities required per step is smaller. This leads to an additional computational overhead for CT-MQC compared to AIMS.

5 Ring-opening process in oxirane

Our simulations start at the time in which, upon absorbing a photon, an oxirane molecule is photoexcited from its ground electronic state S_0 to the lowest-lying bright state, S_2. Such photoexcitation induces ultrafast rearrangements of the molecular structure that eventually drive the system through a conical intersection between S_2 and S_1 within 7 to 15 fs according to TSH and CT-MQC [46]. This process is illustrated in Fig. 1, which shows (in the upper panel) the average population of the electronic states. When the molecule reaches the intersection seam, we observe population transfer from S_2 (fully populated at time $t = 0$) to the first excited state S_1, which is completed after about 25 fs. After that, the dynamics carriers on until a conical intersection between S_1 and S_0 is eventually reached. However, this second event will not be further discuss in this work.

Slightly different results are obtained when employing Ehrenfest dynamics, as the transfer does not involve a complete population transfer from S_2 to S_1. However, the time scale of the crossing of the conical intersection agrees closely with the one obtained with CT-MQC. This does not come as a surprise, as a single crossing event is in general easy to capture in terms of electronic populations. Furthermore, the additional term in the electronic time-evolution of CT-MQC (Eq. (13)), which includes effects beyond Ehrenfest theory, only builds up during and after the nonadiabatic event, meaning that the initial population transfer (before and at the surface crossing) is similar in both CT-MQC and Ehrenfest dynamics.

Additional information about the S_2-to-S_1 transfer process can be extracted from the analysis of the decoherence indicator presented in the lower panel of Fig. 1. The quantity $\eta_{12}(t)$ (black line in Fig. 1), defined by Eq. (22), shows two pronounced peaks, indication that two groups of CT-MQC trajectories funnel through the S_1/S_2 conical intersection at subsequent times. Similarly to previous observations [46] based on surface hopping, we see that also Ehrenfest dynamics is unable to capture the oscillations in the indicator of decoherence and the final decay. In fact, $\eta_{12}(t)$ computed using the Ehrenfest scheme remains constant after the 15 fs of dynamics. The qualitative mismatch with CT-MQC is associated to the lack of decoherence channels in the equation for the evolution of the BO coefficients, $C_k^{(I)}(t)$.

In order to understand if the time delay between different passages through the conical intersection has an effect on the overall dynamics, the indicator of decoherence has been decomposed in different contributions, discriminated according to the nature of the corresponding final molecular configurations. We observe four final product structures, (*i*) a right-open ring structure (observed with probability 36%), (*ii*) a left-open ring structure (observed with

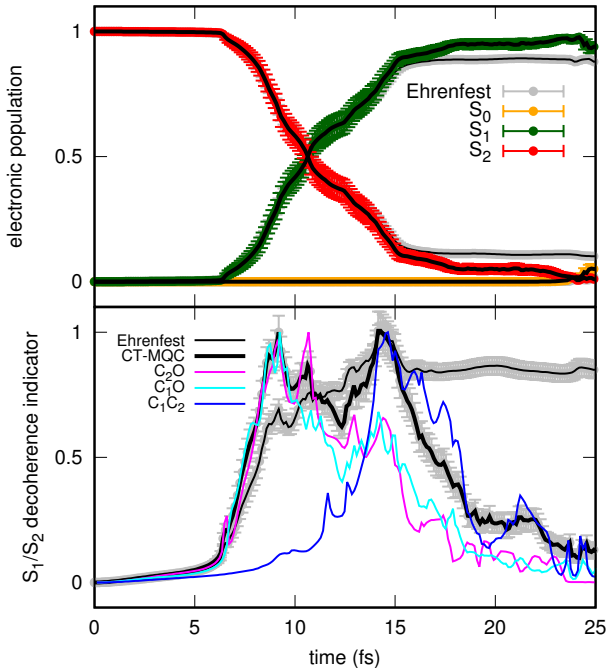

Fig. 1. Upper panel: CT-MQC electronic populations of S_0 (orange), S_1 (dark-green) and S_2 (red) as functions of time. Lower panel: CT-MQC (normalized) indicator of decoherence for the element S_1/S_2 (thick black line), and its decomposition in contributions arising from three sets of trajectories. The trajectory sets labeled with C_1O (cyan line) and C_2O (magenta line) lead to a final configuration where the oxirane ring opens via the breaking of one of the two equivalent CO bonds; the set of trajectories labeled C_1C_2 (blue line) yields final configurations where the ring opens through the elongation of the CC bond. Thin black lines and corresponding grey error-bars refer to Ehrenfest results. The error-bars are evaluated from the standard deviations of the data points.

probability 47%), (*iii*) a CC-extended bond structure (observed with probability 10%), and (*iv*) a closed-ring structure (observed with probability 7%). All reported values are computed as the ratio between the number of trajectories ending up in the target configuration and the total number of trajectories ($N_{tr} = 100$). Structures (*i*) and (*ii*) are equivalent, and we expect that the observed difference in percentage can be reduced by improving the statistics. In these two cases, the ring-opening of oxirane is obtained through the breaking of one of the two CO bonds. In structure (*iii*), the oxirane ring opens via the elongation of the CC bond. A few number of trajectories, identified as structure (*iv*), are not reactive and remains close to the original molecular configuration. For our analysis, we first selected the "reactive trajectories", namely those trajectories yielding the ring-opening of oxirane, and we then decomposed $\eta_{12}(t)$ into contributions associated to the three sets of structures (*i*), (*ii*), and (*iii*). Based on this decomposition, we observe that the first peak (cyan and magenta curves in Fig. 1) between 6 and 12 fs is produced by trajectories that lead to the breakage of one of the two CO bonds. However, these curves do not decay monotonically. Instead, the curves corresponding to the C_1O and C_2O groups both contribute to the second peak (between 12 fs and 17.5 fs), indicating that the first group of trajectories (associated to the first peak) is reached by a second group while funnelling through the conical intersection. The main contribution to the second peak (blue line in Fig. 1) between 12 and 16 fs is however produced by trajectories yielding to a CC bond breaking. These trajectories clearly encounter the nonadiabatic region with some delay when compared to the sets of trajectories of sets (*i*) and (*ii*), and go through the conical intersection in a single step.

The different reaction channels are clearly a consequence of the topology of the TDPES in configuration space. Therefore, we will now scrutinize the TDPES along the different groups of trajectories. We remind that, even though the adiabatic basis has been used to expand the conditional electronic wavefunction of the exact factorization, the nuclear dynamics is still governed by the TDPES and by the time-dependent vector potential of Eq. (3), in their approximate quantum-classical form. The electronic adiabatic basis has been used merely for convenience, as several electronic structure packages are equipped with tools to compute electronic energies, forces and nonadiabatic couplings within this representation of the electronic states.

A representative trajectory has been selected for the groups (*i*) and (*ii*). The populations of the electronic states and the adiabatic potential energy for each configuration visited along the trajectories are reported in Fig. 2 (upper and lower panels, respectively). Fig. 3 shows analogous

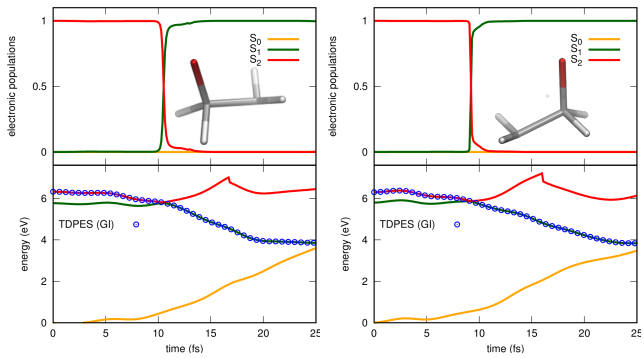

Fig. 2. Upper panels: populations of the electronic states S_0, S_1, and S_2 as functions of time for two selected trajectories of type (*i*) (left) and of type (*ii*) (right). The color code is the same used in Fig. 1. Lower panels: energy profiles (in eV) along the selected trajectories, as in the upper panels. The zero is set to be the value of the energy of S_0 at time $t = 0$. In the upper panels, oxirane at the final time is shown.

results for the groups (*iii*) (left panels) and (*iv*) (right panels). The upper panels of Figs. 2 and 3 confirm that the region of strong coupling between states S_2 and S_1 is encountered by trajectories of type (*i*) and (*ii*) at earlier times when compared to trajectories of type (*iii*). This is also the case for group (*iv*), which undergoes an even slower and smoother transition from S_2 to S_1 than group (*iii*). In fact, the populations of the electronic states cor-

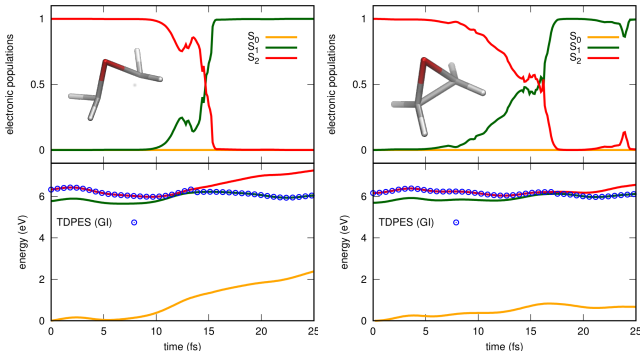

Fig. 3. Same as in Fig. 2, but for the groups of trajectories labeled as (*iii*) (left) and (*iv*) (right).

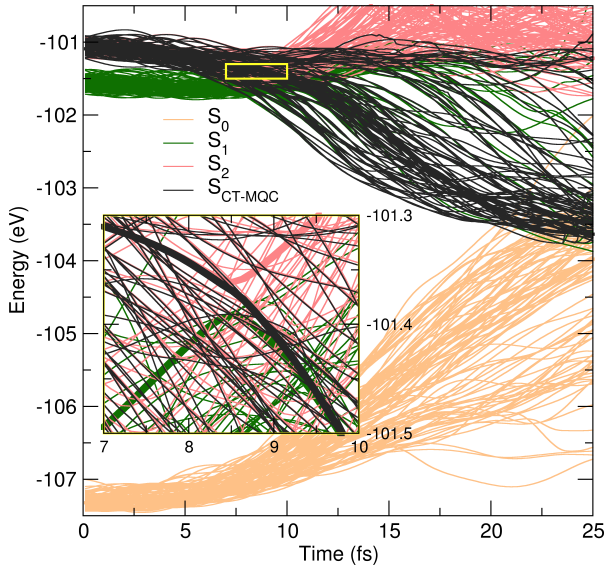

Fig. 4. The time series of the S_0 (orange), S_1 (blue) and S_2 (red) adiabatic PESs computed for a bundle of 100 trajectories started from a ground state thermal ensemble at 300K. The corresponding CT-MQC curves are shown in black. The inset reports a blow-up of the region where most of the S_1/S_2 crossings occur. The thicker lines describe the time evolution of the different PESs for a selected trajectory.

responding to groups (*i*) and (*ii*) sharply switch at the conical intersection at around 10 fs. This behavior is the consequence of the different shapes of the TDPES, represented as dotted lines in Figs. 2 and 3. The trajectories of groups (*iii*) and (*iv*) are driven by a TDPES that is initially flat for about 10-15 fs, following the shape of S_2 adiabatic state, until it smoothly approaches and then switches to S_1. Later, these trajectories continue on S_1 without showing a clear tendency for S_1/S_0 gap closing, pointing towards the presence of a slopped conical intersection between these two states. By contrast, the TDPES sampled by the trajectories of groups (*i*) and (*ii*) follows a steeper path that bring to a fast closure of the S_2/S_1 gap (within about 15 fs) and subsequently of the S_1/S_0 gap (after about 25 fs), suggesting the presence of a funneling process that guides the trajectories to the ground state.

In Fig. 4 we superpose the adiabatic energy profiles for all trajectories (colored lines) and compare them to the TDPES (black lines), computed along the CT-MQC trajectories. We see that while at the initial times the TDPES follows exactly S_2, later the trajectories branch: some remain at an energy similar to the initial one, whereas others rapidly relax and lose nearly 3 eV.

We now move to the analysis of the excited-state dynamics of oxirane as obtained from AIMS. The 20 parent TBFs portray the initial nuclear wavepacket in the second excited-state S_2. Their initial conditions for the CT-MQC dynamics are taken from a subset of those. Upon excitation in S_2, AIMS predicts that the wavepacket approaches rapidly the intersection seam and continues in the first excited state, in agreement with what observed using CT-MQC (Fig. 5). While the time window during

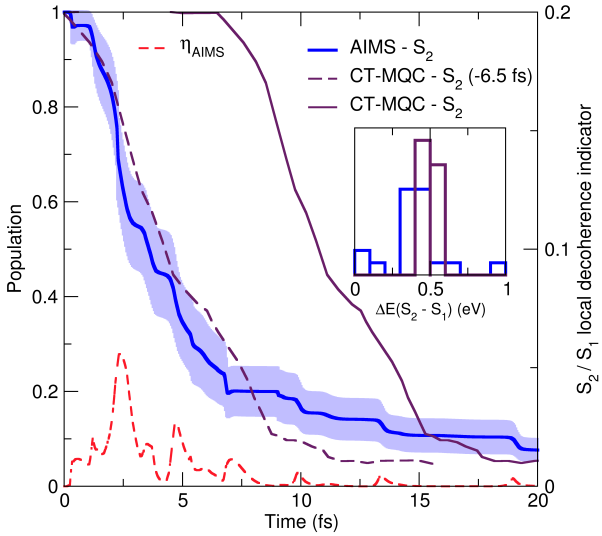

Fig. 5. Time trace of the electronic population in AIMS (blue curve) with corresponding standard error (light blue area). The population obtained with CT-MQC and reported in Fig. 1 is reproduced here for clarity (palatinate line). The dashed palatinate line represents the CT-MQC population curve shifted by -6.5 fs for comparison with the AIMS curve. The inset shows histograms of the S_2/S_1 energy gap of all initial conditions for LR-TDDFT/PBE/TDA/6-31G* (blue) and LR-TDDFT/PBE/TDA/plane-wave (palatinate). The AIMS local decoherence, $\eta_{S_1S_2}^{\text{AIMS}}$, (see text) is indicated with a red dashed line.

which the transfer takes place is nearly identical between the two methods, the AIMS wavepacket appears to reach the intersection seam sooner (by 6.5 fs) than in the case of CT-MQC. This observation is likely related to the different representation of the electronic structure used in the two approches (6-31G* for AIMS and plane waves for CT-MQC), as the S_2-S_1 energy gap distribution at the initial geometries (at $t = 0$) has a larger spread (and is slightly shifted towards smaller values) when using the atom-centered basis set (inset of Fig. 5). As mentioned above, due to the different nature of the AIMS (Gaussian-based method) and CT-MQC (trajectory-based) approaches,

we defined a new, local decoherence indicator for AIMS (Eq. (28)). Therefore, care should be taken when comparing these two quantities, $\eta_{kl}(t)$ of Eq. (22) and $\eta_{kl}^{\text{AIMS}}(t)$ of Eq. (28).

The time-evolution of $\eta_{S_1S_2}^{\text{AIMS}}$ (dashed red line in Fig. 5) clearly shows an initial sharp rise that corresponds to the strong overlap of TBFs in the nonadiabatic region at 2.5 fs. This agrees with the first peak observed in CT-MQC (recalling that the CT-MQC results should be shifted by about −6.5 fs in order to allow for a direct comparison with AIMS results). This overlap, however, rapidly decreases when TBFs move away from each other (see also discussion below on the spawning of TBFs), showing how AIMS naturally encodes decoherence effects. Additional peaks are observed, first at a time delay of about 2.5 fs, and later at a slightly larger delays. These revivals can probably be associated to the peak(s) arising from the second group of CT-MQC trajectories (*i*) and (*ii*)and group (*iii*), respectively. Although, due to the different natures of the decoherence indicators, a direct comparison between CT-MQC and AIMS is not possible, AIMS results qualitatively validate the dynamics generated by CT-MQC.

The dynamics of the AIMS nuclear wavepacket is analyzed by projecting the TBFs onto the two degrees of freedom associated with the CO bonds in oxirane. In Fig. 6 (right), each TBF is represented by a line of different color, where the thickness is proportional to the population ($n_I^{(k)}(t)$, see Eq. (27)) carried by the corresponding TBF. This analysis reveals that following the excitation of the nuclear wavepacket in S_2 the CO dissociation is an important relaxation pathway, in close agreement with the findings reported using the CT-MQC and TSH [46] approaches. We also observe that the breaking of a single CO bond is the dominating deexcitation channel (the inset of Fig. 6 depicts the set of molecular structures at the spawning points and highlights a distribution of CO bond stretches where the spawns, and therefore nonadiabatic transitions, can take place.). A few TBFs exhibit a concerted elongation of both CO bonds (diagonal in Fig. 6, right), but they only carry a rather small population amplitude. Overall, the dynamics of the nuclear wavepacket in AIMS is therefore in good agreement with the dynamics observed with CT-MQC (Fig. 6, left), where the largest fraction of the coupled trajectories also follows a single CO bond dissociation.

In contrast to CT-MQC, AIMS is based on the Born-Huang representation of the molecular wavefunction (see Section 3). As such, the TBFs picture nuclear amplitudes evolving on different time-independent electronic states. When reaching a region of strong nonadiabatic coupling (*i.e.*, when reaching a region where the energy difference between two electronic states becomes small) a parent TBF has the possibility, if necessary, to spawn a new function on the coupled state. This spawn leads to an increase of the number of TBFs, and not to a hop of the TBF from one state to the other. Hence, a spawned TBF will follow its own classical dynamics under the action of the driving state on which it was created. This spawning procedure allows for an amplitude transfer between the two states and to account for decoherence effects between the wavepacket on two PESs. To exemplify the spawning procedure and to contrast it with the TDPES of the CT-MQC dynamics discussed above, we present the AIMS dynamics of one parent TBF (S_2), leading to three spawns to the S_1 state. In the lower panel of Fig. 7, $\text{TBF}_1^{(S_2)}$ represents the parent TBF initiated at $t = 0$ on S_2. It first spawns a TBF on S_1 after 2.3 fs of dynamics (orange line with gray circles), a second one after 10.9 fs (orange line with brown circles), and a third TBF after 14.2 fs (orange line with green circles). Interestingly, this third spawn takes place at a geometry that corresponds to an extended CC bond (larger than 1.7 Å), reminiscent to the swarm of CT-MQC trajectories reaching the intersection seam at later time (see comments to Fig. 1). The lines in Fig. 7 show the potential energy of the TBF evolving in its electronic state and describe their individual dynamics. This comes in strong contrast to TSH, for example, where amplitudes are propagated along a single trajectory. In AIMS, each TBF carries an amplitude and all TBFs are coupled *via* the TDSE.

The overall population of this AIMS run, defined as

$$\rho_{k,\beta}(t) = \sum_{I=1,J=1}^{N_{TBFs,k}^{\beta}} \left(\tilde{C}_{I\beta}^{(k)}(t)\right)^* \tilde{C}_{J\beta}^{(k)}(t) \langle \tilde{\chi}_{I\beta}^{(k)} | \tilde{\chi}_{J\beta}^{(k)} \rangle_{\boldsymbol{R}}\,, \quad (29)$$

is depicted in the upper panel of Fig. 7 and shows the relation between spawned TBFs and population transfers (β here label a specific AIMS run). While AIMS indicates that the nuclear wavepacket rapidly reaches the nonadiabatic region, Fig. 7 shows that additional spawning events, *i.e.*, population transfer, can take place at later times, as observed in the CT-MQC dynamics.

6 Conclusions

In this work, we presented a detailed analysis of the photo-initiated ring-opening process in oxirane based on CT-MQC dynamics, namely the trajectory-based algorithm derived from the Exact Factorization. In particular, we demonstrated the capability of the algorithm to capture decoherence effects related to the nonadiabatic character of the electron-nuclear dynamics in the vicinity of a conical intersection. To this end, we compared the CT-MQC dynamics with Ehrenfest results, proving that the missing ingredient for decoherence in Ehrenfest is associated to the coupling among the trajectories. In fact, CT-MQC equations merely add an additional term to Ehrenfest equations, which tracks the spreading of the trajectories. The inclusion of such correction is sufficient to induce quantum decoherence.

The indicator of decoherence, introduced to prove the qualitative difference between Ehrenfest and CT-MQC, shows oscillations that have been related to the different reaction channels followed by the trajectories, which lead to the different photoproducts. A validation of the CT-MQC approach has been obtained using Ab Initio

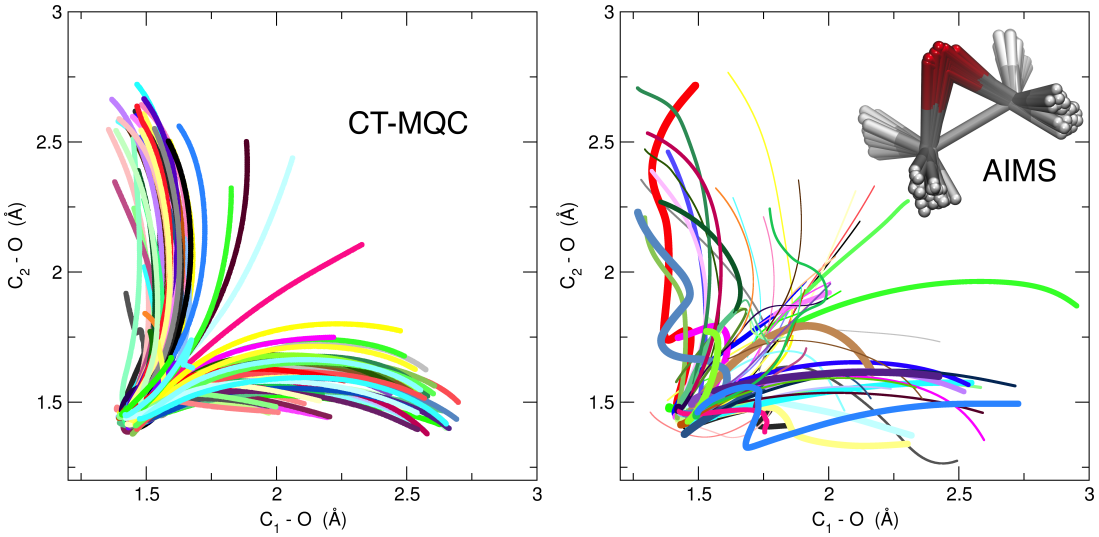

Fig. 6. Projection of the CT-MQC trajectories (left) or the AIMS TBFs (right) onto the two different C-O bonds of oxirane. For the AIMS plot, the thickness of each line is proportional to the normalized incoherent population of TBF I evolving on state k, $n_I^{(k)}(t)$. Note that propagation time of each trajectory/TBFs can be different. The inset (right) presents all the S_2/S_1 spawned AIMS geometries.

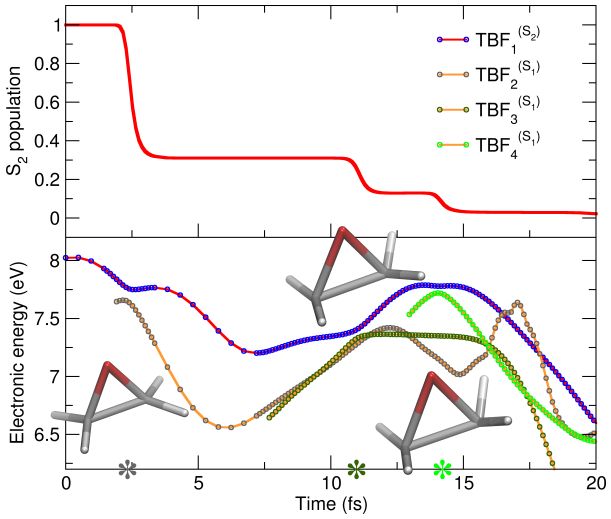

Fig. 7. Example of a typical AIMS run. Upper panel: population of the S_2 state ($\rho_{S_2,\beta}$) for this run β. Lower panel: electronic energies for each of the first four TBFs. $\mathrm{TBF}_1^{(S_2)}$ is the parent TBF initiated at $t = 0$ on S_2 (red line with blue circles) that is spawning three TBFs: $\mathrm{TBF}_2^{(S_1)}$ (orange line with gray circles), $\mathrm{TBF}_3^{(S_1)}$ (orange line with brown circles), $\mathrm{TBF}_4^{(S_1)}$ (orange line with green circles). Each spawning time is highlighted by a colored star on the time axis and the corresponding molecular geometry is given as inset.

Multiple Spawning, a trajectory-based approach to nonadiabatic dynamics able to treat decoherence effects. The good agreement between AIMS and CT-MQC, given the difference in basis set employed, appears to validate the interpretation of the ring-opening process based on CT-MQC. This work therefore provides a first appraisal of the CT-MQC method for the description of nonadiabatic molecular dynamics processes.

Authors contributions

All authors were involved in the preparation of the manuscript. All authors have read and approved the final manuscript.

Acknowledgments

The authors would like express their gratitude to Hardy for his continuing scientific inspiration and friendship.

References

1. R. Kapral, G. Ciccotti, J. Chem.Phys. **110**, 8916 (1999)
2. F. Agostini, S. Caprara, G. Ciccotti, Europhys. Lett. **78**, 30001 (2007)
3. T. Yonehara, K. Hanasaki, K. Takatsuka, Chem. Rev. **112**, 499 (2012)
4. J.C. Tully, J. Chem. Phys. **137**, 22A301 (2012)
5. M. Vacher, M.J. Bearpark, M.A. Robb, J.P. Malhado, Physical Review Letters **118**, 083001 (2017)
6. M.Born, R.J. Oppenheimer, Annalen der Physik **389**, 457 (1927)
7. C. Xie, C.L. Malbon, D.R. Yarkony, D. Xie, H. Guo, J. Am. Chem. Soc. **0**, 10.1021/jacs.7b11489 (2018)
8. A. Scherrer, F. Agostini, D. Sebastiani, E.K.U. Gross, R. Vuilleumier, Phys. Rev. X **7**, 031035 (2017)
9. A. Schild, F. Agostini, E.K.U. Gross, J. Phys. Chem. A **120**, 3316 (2016)
10. A. Scherrer, F. Agostini, D. Sebastiani, E.K.U. Gross, R. Vuilleumier, J. Chem. Phys. **143**, 074106 (2015)

11. L. Wang, A. Akimov, O.V. Prezhdo, J. Phys. Chem. Lett. **7**, 2100 (2016)
12. B.F.E. Curchod, U. Rothlisberger, I. Tavernelli, ChemPhysChem **14**, 1314 (2013)
13. I. Tavernelli, Acc. Chem. Res. **48**, 792 (2015)
14. J.E. Subotnik, A. Jain, B. Landry, A. Petit, W. Ouyang, N. Bellonzi, Ann. Rev. Phys. Chem. **67**, 387 (2016)
15. J.C. Tully, J. Chem. Phys. **93**, 1061 (1990)
16. J.C. Tully, Faraday Discuss. **110**, 407 (1998)
17. J.C. Tully, Faraday Discuss. **110**, 407 (1998)
18. F. Agostini, S.K. Min, A. Abedi, E.K.U. Gross, J. Chem. Theory Comput. **12**, 2127 (2016)
19. M. Ben-Nun, J. Quenneville, T.J. Martínez, J. Phys. Chem. A **104**, 5161 (2000)
20. E. Tapavicza, I. Tavernelli, U. Rothlisberger, Phys. Rev. Lett. **98**, 023001 (2007)
21. B.F.E. Curchod, T.J. Penfold, U. Rothlisberger, I. Tavernelli, Phys. Rev. A **84**, 042507 (2011)
22. A. Abedi, F. Agostini, E.K.U. Gross, Europhys. Lett. **106**, 33001 (2014)
23. F. Agostini, A. Abedi, E.K.U. Gross, J. Chem. Phys. **141**, 214101 (2014)
24. N.L. Doltsinis, D. Marx, Phys. Rev. lett. **88**, 166402 (2002)
25. A.W. Jasper, S. Nangia, C. Zhu, D.G. Truhlar, Acc. Chem. Res. **39**, 101 (2006)
26. B.F.E. Curchod, I. Tavernelli, U. Rothlisberger, Phys. Chem. Chem. Phys. **13**, 3231 (2011)
27. P. Huo, D.F. Coker, J. Chem. Phys. **137**, 22A535 (2012)
28. R. Mitrić, J. Petersen, V. Bonačić-Koutecký, Phys. Rev. A **79**, 053416 (2009)
29. M. Richter, P. Marquetand, J. González-Vázquez, I. Sola, L. González, J. Chem. Theory Comput. **7**, 1253 (2011)
30. R. Kapral, Annu. Rev. Phys. Chem. **57**, 129 (2006)
31. E.R. Dunkel, S. Bonella, D.F. Coker, J. Chem. Phys. **129**, 114106 (2008)
32. T.J. Martínez, M. Ben-Nun, R.D. Levine, J. Phys. Chem. **100**, 7884 (1996)
33. T.J. Martínez, R.D. Levine, J. Chem. Soc., Faraday Trans. **93**, 941 (1997)
34. M. Ben-Nun, T.J. Martínez, J. Chem. Phys. **108**, 7244 (1998)
35. M.D. Hack, A.M. Wensmann, D.G. Truhlar, M. Ben-Nun, T.J. Martínez, J. Chem. Phys. **115**, 1172 (2001)
36. M. Ben-Nun, T.J. Martínez, Advances in Chemical Physics **121**, 439 (2002)
37. B.F.E. Curchod, C. Rauer, P. Marquetand, L. González, T. Martínez, The Journal of Chemical Physics **144**, 101102 (2016)
38. A.M. Virshup, C. Punwong, T.V. Pogorelov, B.A. Lindquist, C. Ko, T.J. Martínez, J. Phys. Chem. B **113**, 3280 (2008)
39. F.F. de Carvalho, M.E.F. Bouduban, B.F.E. Curchod, I. Tavernelli, Entropy **16**, 62 (2014)
40. A. Abedi, F. Agostini, Y. Suzuki, E.K.U. Gross, Phys. Rev. Lett **110**, 263001 (2013)
41. F. Agostini, A. Abedi, Y. Suzuki, E.K.U. Gross, Mol. Phys. **111**, 3625 (2013)
42. F. Agostini, A. Abedi, Y. Suzuki, S.K. Min, N.T. Maitra, E.K.U. Gross, J. Chem. Phys. **142**, 084303 (2015)
43. A. Abedi, N.T. Maitra, E.K.U. Gross, Phys. Rev. Lett. **105**, 123002 (2010)
44. A. Abedi, N.T. Maitra, E.K.U. Gross, J. Chem. Phys. **137**, 22A530 (2012)
45. S.K. Min, F. Agostini, E.K.U. Gross, Phys. Rev. Lett. **115**, 073001 (2015)
46. S.K. Min, F. Agostini, I. Tavernelli, E.K.U. Gross, J. Phys. Chem. Lett. **8**, 3048 (2017)
47. G. Granucci, M. Persico, J. Chem. Phys. **126**, 134114 (2007)
48. A.W. Jasper, S. Nangia, C. Zhu, D.G. Truhlar, Acc. Chem. Res. **39**, 101 (2006)
49. H.M. Jaeger, S. Fischer, O.V. Prezhdo, J. Chem. Phys. **137**, 22A545 (2012)
50. J.E. Subotnik, W. Ouyang, B.R. Landry, J. Chem. Phys. **139**, 214107 (2013)
51. X. Gao, W. Thiel, Phys. Rev. E **95**, 013308 (2017)
52. B.J. Schwartz, E.R. Bittner, O.V. Prezhdo, P.J. Rossky, J. Chem. Phys. **104**, 5942 (1996)
53. J.Y. Fang, S. Hammes-Schiffer, J. Phys. Chem. A **103**, 9399 (1999)
54. N. Shenvi, J.E. Subotnik, W. Yang, J. Chem. Phys. **134**, 144102 (2011)
55. N. Shenvi, J.E. Subotnik, W. Yang, J. Chem. Phys. **135**, 024101 (2011)
56. N. Shenvi, W. Yang, J. Chem. Phys. **137**, 22A528 (2012)
57. J.E. Subotnik, N. Shenvi, J. Chem. Phys. **134**, 024105 (2011)
58. J.E. Subotnik, N. Shenvi, J. Chem. Phys. **134**, 244114 (2011)
59. I. Tavernelli, Phys. Rev. B **73**, 094204 (2006)
60. J.L. Alonso, J. Clemente-Gallardo, P. Echeniche-Robba, J.A. Jover-Galtier, J. Chem. Phys. **139**, 087101 (2013)
61. A. Abedi, N.T. Maitra, E.K.U. Gross, J. Chem. Phys. **139**, 087102 (2013)
62. F. Agostini, S.K. Min, E.K.U. Gross, Ann. Phys. **527**, 546 (2015)
63. F.G. Eich, F. Agostini, J. Chem. Phys. **145**, 054110 (2016)
64. B.F.E. Curchod, F. Agostini, E.K.U. Gross, J. Chem. Phys. **145**, 034103 (2016)
65. B.F.E. Curchod, F. Agostini, J. Phys. Chem. Lett. **8**, 831 (2017)
66. E. Khosravi, A. Abedi, A. Rubio, N.T. Maitra, Phys. Chem. Chem. Phys. **DOI: 10.1039/c6cp08539c** (2017)
67. Y. Suzuki, K. Watanabe, Phys. Rev. A **94**, 032517 (2016)
68. Y. Suzuki, A. Abedi, N.T. Maitra, K. Yamashita, E.K.U. Gross, Phys. Rev. A **89**, 040501(R) (2014)
69. E. Khosravi, A. Abedi, N.T. Maitra, Phys. Rev. Lett. **115**, 263002 (2015)
70. S.K. Min, A. Abedi, K.S. Kim, E.K.U. Gross, Phys. Rev. Lett. **113**, 263004 (2014)
71. R. Requist, F. Tandetzky, E.K.U. Gross, Phys. Rev. A **93**, 042108 (2016)
72. P.R. Holland, *The Quantum Theory of Motion - An Account of the de Broglie-Bohm Causal Interpretation of Quantum Mechanics* (Cambridge University Press, 1993)
73. B.F.E. Curchod, T.J. Martínez, Chem. Rev. p. in press (2018)
74. E.J. Heller, The Journal of Chemical Physics **75**, 2923 (1981)
75. S. Yang, J.D. Coe, B. Kaduk, T.J. Martínez, The Journal of chemical physics **130**, 04B606 (2009)
76. B. Mignolet, B.F.E. Curchod, arXiv:1801.06639 (2018)
77. B.G. Levine, J.D. Coe, A.M. Virshup, T.J. Martinez, Chemical Physics **347**, 3 (2008)
78. J.W. Snyder Jr, B.F.E. Curchod, T.J. Martínez, The journal of physical chemistry letters **7**, 2444 (2016)

79. H. Tao, B.G. Levine, T.J. Martínez, J. Chem. Phys. A **113**, 13656 (2009)
80. S. Pijeau, D. Foster, E.G. Hohenstein, The Journal of Physical Chemistry A **121**, 4595 (2017)
81. B.F.E. Curchod, A. Sisto, T.J. Martínez, The Journal of Physical Chemistry A **121**, 265 (2017)
82. CPMD, *http://www.cpmd.org/, Copyright IBM Corp 1990-2015, Copyright MPI für Festkörperforschung Stuttgart 1997-2001.*
83. J.P. Perdew, K. Burke, M. Ernzerhof, Phys. Rev. Lett. **77**, 3865 (1996)
84. E. Runge, E.K.U. Gross, Phys. Rev. Lett. **52**, 997 (1984)
85. M. Petersilka, U.J. Gossmann, E.K.U. Gross, Phys. Rev. Lett. **76**, 1212 (1996)
86. M.E. Casida, *Time-dependent density-functional response theory for molecules*, in *Recent Advances in Density Functional Methods*, edited by D.P. Chong (Singapore, World Scientific, 1995), p. 155
87. I. Tamm, J. Phys **9**, 449 (1945)
88. S.M. Dancoff, Phys. Rev. **78**, 382 (1950)
89. C.A. Ullrich, *Time-Dependent Density-Functional Theory* (Oxford University Press, 2012)
90. B.G. Levine, C. Ko, J. Quenneville, T.J. Martinez, Mol. Phys. **104**, 1039 (2006)
91. E. Tapavicza, I. Tavernelli, U. Rothlisberger, C. Filippi, M.E. Casida, J. Chem. Phys. **129**, 124108 (2008)
92. L. Kleinman, D.M. Bylander, Phys. Rev. Lett. **48**, 1425 (1982)
93. C.M. Isborn, N. Luehr, I.S. Ufimtsev, T.J. Martínez, J. Chem. Theory Comput. **7**, 1814 (2011)
94. I.S. Ufimtsev, T.J. Martinez, J. Chem. Theory Comput. **4**, 222 (2008)
95. I.S. Ufimtsev, T.J. Martinez, Journal of Chemical Theory and Computation **5**, 1004 (2009)
96. I.S. Ufimtsev, T.J. Martinez, J. Chem. Theory Comput. **5**, 2619 (2009)
97. R. Ditchfield, W.J. Hehre, J.A. Pople, J. Chem. Phys. **54**, 724 (1971)